Surfactant- and Aqueous-Foam-Driven Oil Extraction from Micropatterned Surfaces

Rémy Mensire, Jason S. Wexler, Augustin Guibaud, Elise Lorenceau, Howard A. Stone

Surfactant and aqueous foam-driven oil extraction from micropatterned surfaces

Rémy Mensire,[†,‡] Jason S. Wexler,[‡] Augustin Guibaud,[¶] Elise Lorenceau,[†] and Howard A. Stone[*,‡]

†*Université Paris-Est, Laboratoire Navier, UMR 8205 CNRS-ENPC-IFSTTAR - 2 allée Kepler F-77420 Champs-sur-Marne, France*

‡*Department of Mechanical and Aerospace Engineering, Princeton University, Princeton, New Jersey 08544, United States*

¶*Department of Physics, Ecole Polytechnique, 91120 Palaiseau, France*

E-mail: hastone@princeton.edu

Abstract

Liquid-infused surfaces are rough or patterned surfaces in which a lubricating fluid, such as oil, is infused, which exhibits various original properties (omniphobicity, biofouling, drag reduction). Indeed, the outer flow can entrain the oil trapped between the pattern of the surfaces by shearing the oil-water interface and cause the loss of the omniphobic properties of the interface. Starting from the theoretical analysis of Wexler et al.[1] (*Phys. Rev. Lett.* **2015**, *114*, 168301), where a pure aqueous solution is the outer phase, we extend the predictions by introducing an extraction efficiency parameter α and by accounting for new dynamical effects induced by surfactants and aqueous foams. For surfactant solutions, decreasing the oil-water interfacial tension γ_{ow} not only enhances oil extraction as expected but also modifies the dynamics of the receding oil-water interface through the variations of the receding contact angle θ

with the capillary number Ca, which is the ratio between the viscous and the capillary forces at the oil-water interface. For aqueous foams, the extraction dynamics are also influenced by the foam flow: oil is sheared by the thin film between the bubbles and the lubricating layer, which imposes a stronger interfacial shear compared to pure aqueous solutions. In both surfactant and foam cases, the experimental observations show the existence of non-uniform extraction dynamics related to the surfactant-induced instability of a two-fluid shear flow.

Keywords

Surfactants, Aqueous foams, Liquid-infused surfaces

Introduction

Liquid-infused surfaces are rough or patterned surfaces in which a lubricating liquid is infused. They have been studied in recent years for their useful properties, such as omniphobicity, biofouling and drag reduction[2–9] where they interact with an immiscible liquid droplet or a dynamic fluid environment. Yet, they can lose their properties if the lubricating layer vanishes. The failure of these surfaces under stress tangent to the surface has been investigated by Wexler et al.,[1] who studied the drainage or the retention of the lubricating liquid under the shear-driven action induced by the flow of a pure aqueous phase. In this paper, we extend their work by considering aqueous liquids containing surfactants and foams. This step builds upon earlier work by Jacobi et al.,[10] who highlighted that traces of surfactants could induce unusual drainage behavior.

Since fluid is removed from cavities during the failure of liquid-infused surfaces under external shear flow, this configuration can help understand complex problems, such as oil recovery from a rough surface or soil remediation upon contamination by a liquid pollutant.[11,12] In these examples, surfactants and aqueous foams are commonly used.[13–20]

However, due to the high degree of complexity of the soil, simpler configurations, such as a soil column or a millifluidic porous soil model with a controlled pore size are often considered. Such studies provide qualitative insight and quantitative results. In all those studies, the oil is trapped in the volume of the porous media. Our approach and configuration are different since we consider geometries where the oil is trapped in the roughness of the surface of the material and the processes by which the oil can be remobilized if not completely removed. Ideally, there would be great value to predict the efficiency of the recovery process according to parameters such as roughness size, mean bubble radius and injection rate. Thus, studying the drainage of oil from liquid-infused surfaces can shed insight on liquid recovery phenomena from rough porous media.

In the work below, we model and build our system as a single channel connected to different oil-filled micropores of a textured surface (Fig. 1a). We study theoretically and experimentally the effects of surfactant solutions and aqueous foams on the extraction efficiency of different oils trapped within the pores of the textured surface. We develop and use a mathematical model introduced by Wexler et al.,[1] and compare theoretical predictions to experimental results in the case where the external flow consists of a surfactant solution or an aqueous foam. We define a quantitative parameter, the extraction efficiency,[13] as the percentage of recovered oil, and study the extraction dynamics, which strongly depend on the physical and chemical properties of the oil-water interface.

Surfactant-driven oil extraction

Experimental section

We choose an array of microfabricated and equally-spaced posts to study the drainage of liquid-infused surfaces when the external shear flow contains surfactants. The patterned geometry is imprinted on the upper side of a microfluidic channel, as shown in Fig. 1. The system mimics a rough surface containing trapped liquid, where the assembly of posts

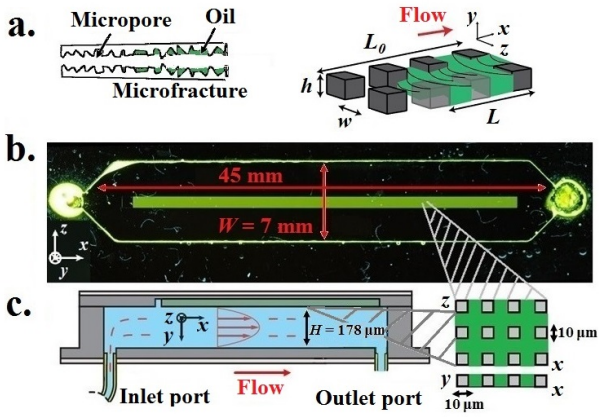

Figure 1: Geometry of the microfluidic channel with the liquid-infused micropattern imprinted on the upper side of the channel. a. Analogy between a real microfracture or a rough surface trapping a liquid phase and a liquid-infused substrate. b. Top-view of the channel, with the oil fluorescing green-yellow. c. Side-view of the channel consisting of one wall with an array of posts.

represents a set of oil-filled and connected pores, which is a feature of randomly rough systems with open pores.

The materials and the microfabrication are the same as those used by Wexler et al.[1] and are sketched in Fig. 1b-c. The pattern and the channel, lying on black borosilicate glass, are molded in an epoxy adhesive (Norland Optical Adhesive 81) by the "sticker technique".[21] The channels are 7 mm wide, 178 or 89 µm high, and 45 mm long. The channel has two ports: one inlet port at the upstream end and one outlet port at the downstream end. The 36 mm long and 1 mm wide pattern is located near the centerline of the channel and aligned with the inlet and outlet ports at a distance of 5 mm from both ports. The pattern consists of cubic posts (10 μm on a side), which are equally spaced at a distance of 10 μm, and ends with a 1 mm by 1 mm open well for flow entry (Fig. 1b).

The characteristics of the tested fluids are summarized in Table 1, with the dynamic viscosities measured in a rheometer (Anton-Paar) with a cone-plate geometry. The outer fluid is a surfactant solution. We use two types of surfactants: either SDS (sodium dodecyl sulfate) with different concentrations from 0.1 g/L to 10 g/L (cmc $\approx$ 2 g/L), or a combination of co-surfactants, CAPB (cocoamidopropylbetaine), SLES (sodium laurylethyl sulfate), Mac (myristic acid) and 10 wt% glycerol[24,25] with different surfactant concentrations from

Table 1: Characteristics of the aqueous solution - oil combinations. Here, η_w (mPa.s) and η_o (mPa.s) are, respectively, the shear viscosity of water and oil.

Aqueous solution - Oil	η_w	η_o
CAPB+SLES+MAc+10% glycerol - Olive oil (O)	1.4	68.5
CAPB+SLES+MAc+10% glycerol - Silicon oil 1 (PDM-7050 - S1)	1.4	201
CAPB+SLES+MAc+10% glycerol - Silicon oil 2 (PDM-7040 - S2)	1.4	42.7
SDS - Olive oil	1	68.5

0.005 wt% to 2 wt% (cmc $\approx$ 0.1 wt%). The lubricating oils, which initially fill the patterned substrate, are olive oil (commercial and Sigma-Aldrich) and two silicon oils (Gelest PDM - 7040 and 7050) containing a small amount of fluorescent dyes (from Tracerline) (1:100). In the following, all the interfacial tensions are measured by the pendant drop technique with a precision of $\pm$ 0.5 mN/m. Fig. 2 presents the variations of the equilibrium oil-water interfacial tension γ_{ow} with the surfactant concentration c. As expected, γ_{ow} decreases when c increases with the cmc $\approx$ 2 g/L in both SDS-olive oil and CAPB-SLES-Mac-olive oil cases. As explained below, we clear the surfactant solution from the channel at a very slow velocity (0.002 mL/min) to leave oil trapped in the texture of the surface. Thus, we give time for the system to equilibrate in terms of surfactant dynamics, which allows us to use the values presented in Fig. 2.

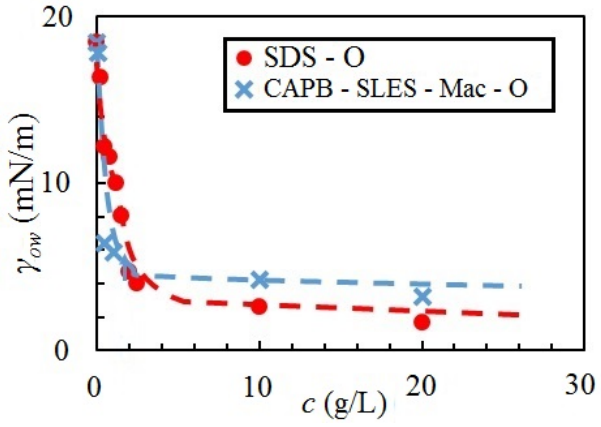

Figure 2: Equilibrium oil-water interfacial tension γ_{ow} as a function of the surfactant concentration c for SDS-Olive oil (O) and CAPB-SLES-Mac-Olive oil (O) combinations. The blue and the red dashed lines are guide lines. The error margin on the interfacial tension is $\pm$ 0.5 mN/m.

At the start of an experiment, the channel is completely filled with oil from the down-

stream port. Then, the entire channel is cleared by the flow of the outer aqueous phase at a low injection rate (0.002 mL/min), which leaves oil trapped between the posts: the texture is oil-wet. The oil in excess is evacuated to a reservoir from the outlet port. This procedure prevents oil extraction from being disturbed by an excess of oil. Once the main channel is cleared of oil, the outer fluid is injected at a constant flow rate between 0.05 mL/min and 8 mL/min, corresponding to average flow speeds. The experimental observations are made under UV or blue light (with a yellow filter from Tiffen in front of the camera objective) to ensure a strong contrast between the black glass background and the fluorescent oil trapped in the pores.

Snapshots of the oil extraction process are taken every minute. A typical time series of the oil extraction pattern is shown in Fig. 3. Depending on the flow rate Q and the oil-water interfacial tension γ_{ow}, the process shows two different patterns. In one case, for sufficiently low Q and high γ_{ow}, the draining front advances uniformly, as observed previously by Wexler et al. with pure aqueous solutions.[1] We define a retention length $L(t)$ (t is the time) and a steady-state retention length L_∞ (Fig. 1a). In a second case, for sufficiently high Q and low γ_{ow}, the draining front still propagates along the flow direction but is more irregular, leaving oil patches behind it. Since it is difficult to define a retention length in this second situation, we introduce the extraction efficiency α to quantify oil extraction from the porous substrate. Specifically, we define $\alpha = V_d/V_0$ which is the ratio between the volume of extracted oil V_d and the initial volume of oil V_0 between the posts. The parameter α varies from 0, when the pores are completely filled, to 1, when they are completely empty. In the cases depicted in Fig. 3, oil leaves the texture by either (a) overflow out of the pattern (stain-like oil downstream, as observed in Jacobi et al.[10]) (b) or small filaments with a diameter of the order of the distance between the posts, which eventually destabilize into tiny droplets.

To measure $\alpha(t)$, we record the fluorescence intensity I in the pattern by using the sum of grey levels after image processing with ImageJ software. Neglecting photobleaching that

occurs for a timescale longer than our experimental time, we assume that the fluorescence level is approximately proportional to the volume of the remaining oil $V_0 - V_d$, since the depth of the posts is small. Given that light conditions can change from one experiment to another, we only have access to $\alpha \approx 1 - I/I_0$, where I_0 is the initial fluorescence intensity between the posts for each experiment. In Fig. 4, we report α as a function of time t for the different liquids.

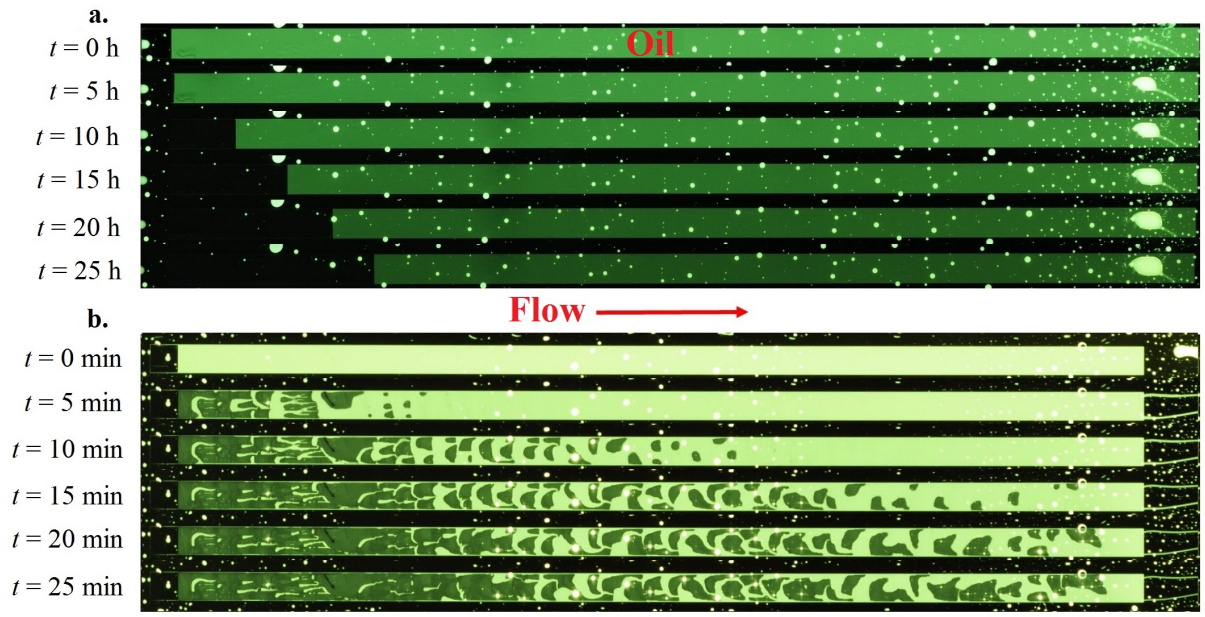

Figure 3: Top views of typical oil extractions (olive oil) by a surfactant solution (CAPB - SLES - Mac - 10 wt% glycerol). Fluorescent dyed oil appears green-yellow. The small green-yellow dots correspond to some oil droplets stuck on the epoxy surface when the channel was initially cleared of oil in the first place. The flow is from left to right. a. Extraction with a uniform front; $Q = 0.05$ mL/min and $\gamma_{ow} = 4.2$ mN/m, time interval: 5 h. b. Extraction with an unstable pattern; $Q = 5$ mL/min and $\gamma_{ow} = 4.2$ mN/m, time interval: 5 min.

Results and discussion

When varying one parameter (Q, γ_{ow}, η_o or the channel height H) during flow of a surfactant solution, α follows one typical evolution, as shown in Fig. 4. As time increases, α increases quickly before slowing down and eventually reaching a maximum value α_∞ at long times. For a given time and considering the different possible material properties, we

find that oil recovery is more efficient if interfacial tension is low and the aqueous phase flow rate is high. Efficiency is also enhanced if the oil viscosity and channel height are low.

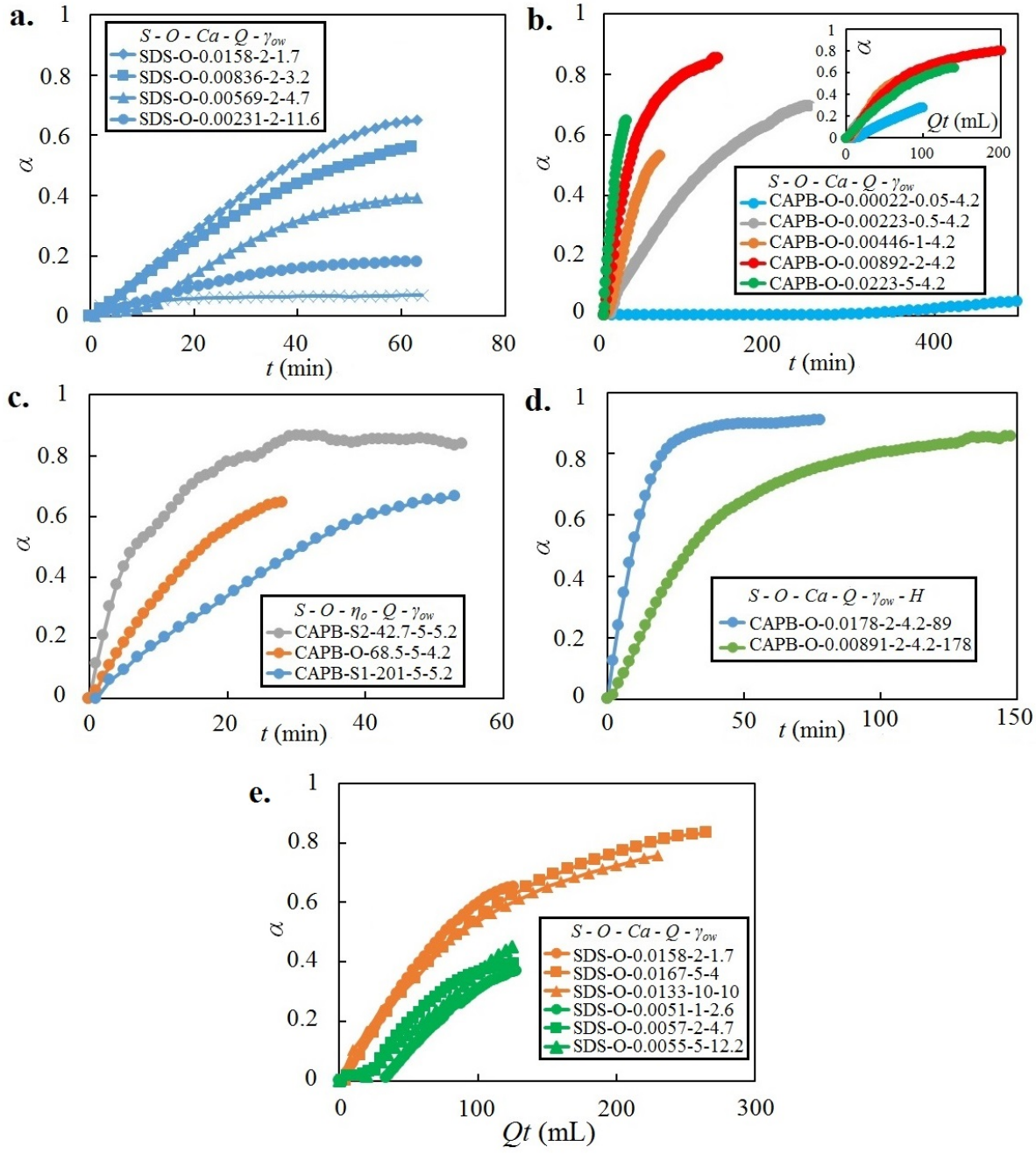

Figure 4: Extraction efficiency α as a function of time t for different draining liquid - oil combinations with the following variable parameters: a. γ_{ow} (mN/m). b. Q (mL/min) (Inset: α as a function of Qt). c. η_o (mPa.s). d. H (µm). S, O and Ca are, respectively, the surfactant type, the oil type and the capillary number defined in (Eq. 2b). e. Extraction efficiency α as a function of the injected volume Qt for SDS - olive oil combination, with $Ca \approx 0.015$ and 0.005.

Next, we report α as a function of the injected volume Qt (Fig. 4e). The data is organized by the capillary number $Ca = \eta_w Q/(WH\gamma_{ow})$, where W is the channel width. The six different data sets in Fig. 4e correspond to two capillary numbers $Ca \approx 0.005$ and $Ca \approx 0.015$. The experimental data, for a given capillary number, collapses on one single curve, suggesting that α depends on Qt and Ca.

Theory

For experiments with a groove geometry, the extraction dynamics were explained by Wexler et al. for pure aqueous solutions as the outer phases.[1] A similar interpretation can be made here. The ratio between the channel width and height is large, 40:1 or 20:1, and the channel is much deeper than the pattern ($H \gg h$). With the low viscosity ratio $\lambda = \eta_w/\eta_o \ll 1$ and the no-slip boundary condition, we can consider a parabolic velocity profile in the outer flow, which corresponds to a planar Poiseuille-like flow[22] for which the shear stress at the oil-water boundary is $\tau_{xy} \approx 6\eta_w Q/(WH^2)$. Gravity is also neglected because the Bond number $Bo = (\rho_w - \rho_o)gw^2/\gamma_{ow} \approx 10^{-6}$ is small, where ρ_w and ρ_o are, respectively, the water and the oil densities. As sketched in Fig. 1a (right), the external flow shears the oil-water interface and drags oil downstream out of the pattern. At short times, the tangential stresses in the water and the oil phase are equal, thus $\tau_{xy} \sim -\frac{\eta_o}{h}\frac{dL}{dt}$, where h is the height of the posts. For such short times, we deduce $\alpha(t) = 1 - L(t)/L_o \sim \tau_{xy} ht/\eta_o$, where L_o is the length of the pattern (see Fig. 1). Locally, the applied shear deforms the oil-water interface, as sketched in Fig. 5. When the dynamic contact angle at this pinned interface reaches the receding contact angle θ, the interface slides to the bottom of the posts.[23]

The deformation of the liquid-liquid interface induces a difference of curvature between the upstream and the downstream ends for longer times. The capillary pressures are $\Delta p_C = p_w - p_o = \gamma_{ow}/r_{min}$ upstream (p_w and p_o are, respectively, the pressures in the outer fluid and the oil phase) and $\Delta p_C = 0$ downstream. The pressure gradient in the aqueous phase

can be written as $dp_w/dx = -12Q\eta_w/WH^3$. Thus, the pressure difference Δp_w between the inlet and the outlet of the channel of length $L_{channel}$ is $\Delta p_w \approx -12Q\eta_w L_{channel}/WH^3 \approx$ 4 x 10^2 Pa for $Q = 2$ mL/min. This value is small compared to the capillary pressure and the pressure difference in the oil phase is directly $\Delta p_o = \gamma_{ow}/r_{min}$. Thus, the pressure p_o in the trapped fluid is lower upstream than downstream and the pressure gradient drives an oil counterflow within the liquid trapped between the posts. We assume that the oil layer percolates through the connected posts. Thus, it is always possible to define a pressure path within the porous system. Oil is being extracted so long as the shear-driven flux is higher than the capillary pressure-driven flux. The maximum efficiency $\alpha_\infty = 1 - L_\infty/L_o$ is reached when the shear-driven flux is exactly balanced by the pressure-driven flux. In terms of stresses, $\tau_{xy}/h \sim (\gamma_{ow}/r_{min})/L_\infty$ and $L_\infty \sim h\gamma_{ow}/(r_{min}\tau_{xy})$ with r_{min} the minimum radius of curvature of the oil-water interface.

Rewriting the complete steady-state solution of Wexler et al.[1] (Eq. (2)), we find a similar result:

$$\alpha_\infty = 1 - \frac{c_p h \gamma_{ow}}{c_s r_{min} \tau_{xy} L_o} \quad , \tag{1}$$

where c_p and c_s are numerical factors linked to the geometry of the channel. We use $r_{min} = w/(2\cos\theta)$ (with w the spacing between posts).

The details of the comprehensive original time-dependent drainage theory, explained by the aforementioned scaling laws, are given in the supplementary material of Wexler et al.[1] Rewriting the time-dependent theory with α(t) and α_∞ as the main variables, we find:

$$\alpha + (1-\alpha_\infty)\log\left(\frac{\alpha_\infty}{\alpha_\infty - \alpha}\right) = \frac{6c_s h \eta_w}{WH^2 c_d L_0 \eta_o} Qt \tag{2a}$$

$$\alpha_\infty = 1 - \frac{c_p H h \cos\theta}{3c_s L_o w Ca} \quad , \tag{2b}$$

where c_d is a numerical factor depending on the receding contact angle θ at the oil-water interface, and we have introduced the capillary number Ca. For our experiments, $w = h$.

Thus, c_d (see Eq. (9) in the supplementary material of Wexler et al.[1]) can be expressed as:

$$c_d = 1 - \frac{1}{2\cos\theta}\left(1 - \frac{1}{2}\sqrt{1-\cos^2\theta}\right) + \frac{1}{4\cos^2\theta}\csc^{-1}\left(\frac{1}{\cos\theta}\right). \tag{3}$$

Subsequently, we deduce θ from the confocal microscope measurements of the interface deflection at different points along the porous substrate, when the pinned oil-water contact line starts receding. We report the values of θ with respect to Ca in Fig. 5 and we notice a systematic variation of θ between 0^o and 90^o. Such a variation has been observed when the contact line is perpendicular to the flow direction and moves streamwise with the flow: this is the well-known Tanner-Hoffmann law[27–30] which relates the variation of the dynamic contact angle θ_d at an air-liquid interface moving across a solid substrate with respect to the capillary number with the finding that $\theta_d \propto Ca^{1/3}$. For liquid-liquid interfaces, Fermigier et al.[26] have observed the same kind of variation and use the "Cox law"[31,32] to model the movement of a glycerin-silicone contact line in a capillary tube, which depends on Ca and the viscosity ratio $\lambda = \eta_w/\eta_o$. In our case, it is difficult to apply the aforementioned model since the contact line recedes transversely to the main flow and θ is defined in the post and flow cross-section, as sketched in Fig. 5d-e. The velocity profile in the vicinity of the contact line is unknown and might not be parallel to the motion of the contact line. However, from our contact angle observations and measurements, a dependence of θ on Ca can be similarly reported.

The coefficient c_d does not change very much, from 0.893 to 0.993, when θ varies from 0^o to 90^o. Considering the small variations of c_d, Eqs. (2a - 2b) are in good agreement with our experimental observations in terms of the dependence in Fig. 4: α depends on Qt, η_o, the geometry of the channel and Ca. With the measured values of θ and the theoretically deduced numerical factors $c_s = 0.0764$, $c_p = 0.0573$, which enable the calculation of α_∞ in Eq. (2b) and c_d from Eq. (3), we rescale the data sets. In Fig. 6a, we represent the experimental efficiency α_{exp} as a function of $g(t) = \frac{6c_s h\eta_w}{WH^2 c_d L_0 \eta_o} Qt$, which is the

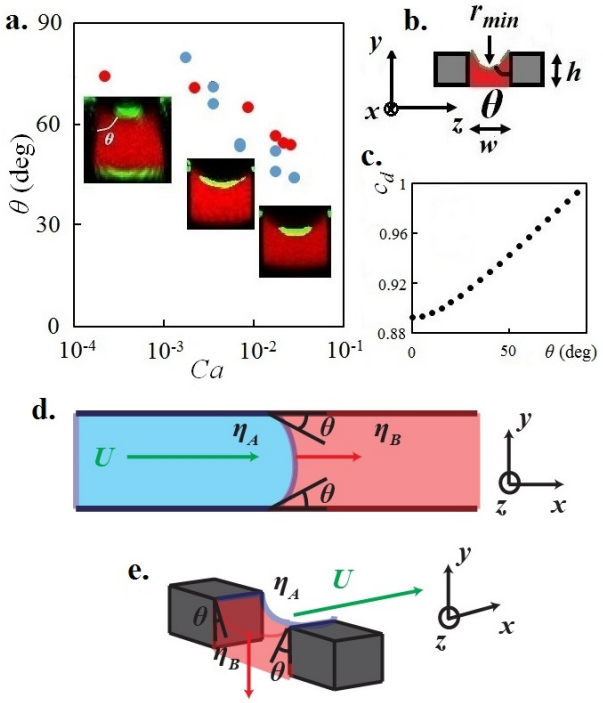

Figure 5: a. Measurements of the receding contact angle θ as a function of Ca for CAPB - olive oil (red dots) and CAPB - silicon oil 1 (blue dots) combinations. Oil appears red in the confocal microscope and the green line is the laser reflection between the glass and the aqueous phase. b. Cross-section of the oil-water interface. c. Evolution of the numerical factor c_d with respect to θ. d. Movement of the A-B interface parallel to the flow of mean velocity $\boldsymbol{U}$ with the viscosity ratio $\eta_B/\eta_A > 1$. e. Movement of the same A-B interface for our post pattern with the interface receding perpendicular to the main flow of mean velocity $\boldsymbol{U}$.

right-hand side of Eq. (2a), with CAPB-SLES-Mac as the outer phase and three different oils as the inner phases. All curves collapse onto a master curve for $\alpha_{exp} < 0.4$ and $g(t) < 0.5$, which suggests that our theory reasonably predicts the linear time dependence of extraction dynamics at short times. To go further, Fig. 6b shows the collapse between $f(\alpha_{exp}) = \alpha_{exp} + (1-\alpha_\infty)\log\left(\frac{\alpha_\infty}{\alpha_\infty - \alpha_{exp}}\right)$ and $g(t)$ for the entire time frame. The predictions of Wexler et al.[1] account for the observed dynamics if we consider a variation of the receding contact angle due to the addition of surfactants, which was not observed with pure solutions.

Extraction instability

As seen in Fig. 3b, the drained front loses its uniformity as Q increases and γ_{ow} decreases, leaving patches of oil between the posts. Fig. 7a shows the instability for both connected

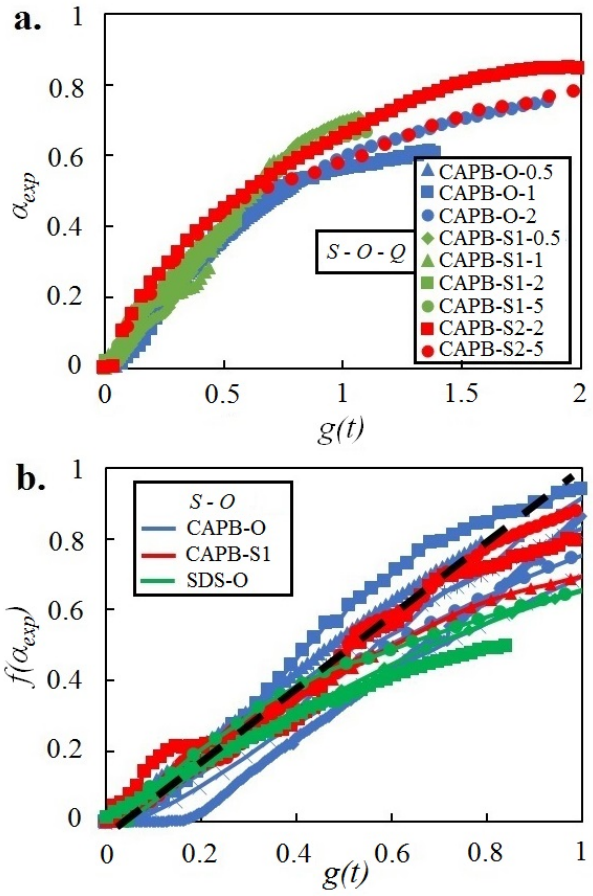

Figure 6: a. Experimental efficiency α_{exp} as a function of $g(t)$ for CAPB - olive oil, CAPB - silicon oil 1 and CAPB - silicon oil 2 combinations. b. $f(\alpha_{exp})$ as a function of $g(t)$ for different surfactant-oil combinations. The black dashed line is the theoretical prediction (Eq. (2a)).

posts and independent grooves, indicating that this instability occurs for multiple types of surface texture. The appearance of these stable and unstable regimes, reported in Fig. 7b, could be caused by the flow of two superposed layers of fluids of different viscosities (the aqueous solution and the underlying oil layer trapped in-between the posts). Indeed, it has been long known that such a two-fluid shear flow can be unstable.[33–35] In particular, when gravity and interfacial tension are neglected, Yih[33] and Hooper et al.[34] have shown that the jump in the velocity profile for two fluid layers of different viscosity causes the development of the instability, in the limit of low Reynolds numbers. Long-wave and short-wave instabilities appear if $\eta_o > \eta_w$ and $h < H - h$. However, in our case, the capillary number is low, so we expect that interfacial tension plays a significant role. The

destabilizing role of surfactants on the interface recalls the work of Frenkel et al.[36] and Blyth et al.[37] who showed that the presence of insoluble surfactants at the interface can trigger the growth of interfacial waves in a two-layer channel flow, even in the absence of inertia, provided that shear flow occurs. From their calculations, a surfactant-free system is stable, which corresponds to the system used by Wexler et al.[1] where the extracting front remains uniform along the section of the post pattern. In the two-layer geometry, the growth rate of the instability increases with the Marangoni number $M \propto C^* / \gamma_{ow}^*$ where C^* and γ_{ow}^* are, respectively, the initial interfacial concentration of surfactants and the initial oil-water interfacial tension. We also observe that very low capillary numbers can be stable as the range of unstable wavenumbers is reduced.[37] But the instability is amplified for very low interfacial tension, like in our experimental observations. Thus, this would be the first experimental observation of the destabilizing role of surfactants in a two-layer channel flow. Yet, other types of two-fluid instabilities can also be considered, such as the fingering instabilities[38] appearing in the transverse direction to the flow for the displacement of a thin film by body or shear forces.

Aqueous foam-driven oil extraction

In the previous section, we studied oil extraction when surfactants are added to the external phase. In this section, we investigate the case where gas is co-injected with surfactants, thus creating an aqueous foam, which also acts to extract the infused liquid during flow.

Experimental section

We first generate an aqueous foam through a flow-focusing device. The flow-focusing technique allows control of bubble size by co-injecting nitrogen gas at a given pressure p and the liquid phase (CAPB - SLES - Mac described for surfactant solutions) at a given flow rate q through a constriction.[39,40] To slow down bubble coarsening, gas is blown through a

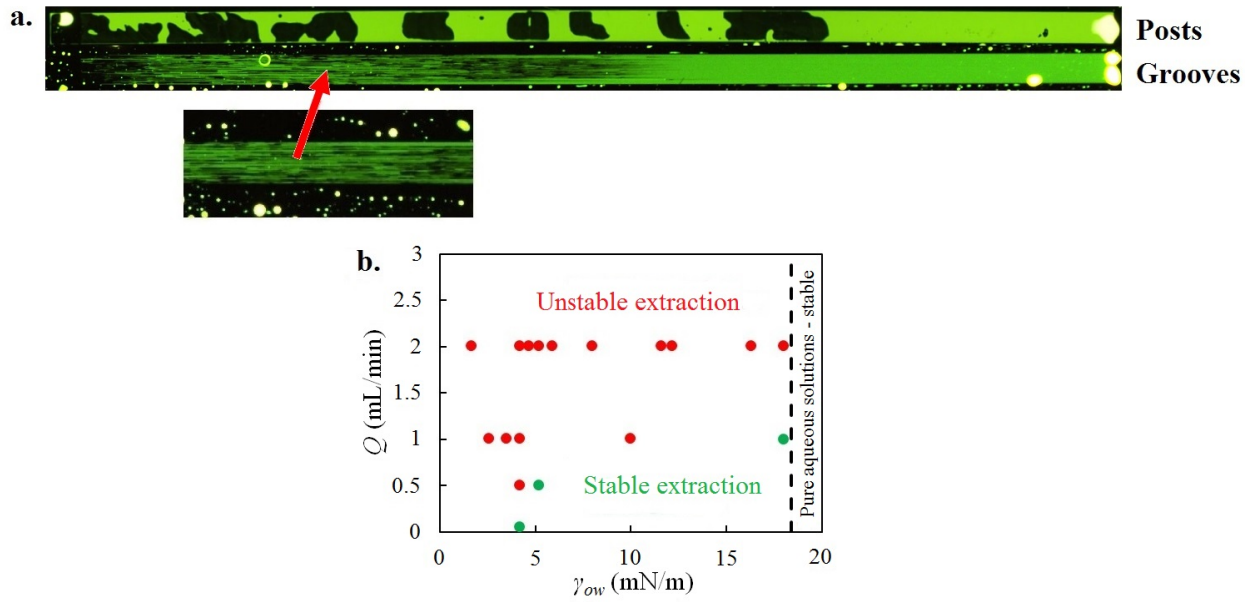

Figure 7: a. Typical unstable extraction pattern for posts and grooves with the same height and width. The surfactant solution - oil combination is SDS (2 g/L) - olive oil; $Q = 2$ mL/min and $t = 60$ min. Contrast is enhanced in the snapshots. b. Phase diagram where each point (γ_{ow}, Q) represents an experiment with the CAPB - olive oil, the CAPB - silicon oil 1 and the SDS - olive oil combinations. Unstable extraction is represented by red dots and stable extraction by green dots. The dashed black line defines the stable regime for pure aqueous solutions - olive oil (the silicon oil 1 case is further to the right of the diagram).

solution of tetradecafluorohexane (C_6F_{14})[41] before entering the device, because fluorinated gas is insoluble in water. We calibrate the mean bubble radius R_b as a function of q and p. Garstecki et al.[39] have shown that the bubble volume V_b scales as $p/(q\eta_w)$. Typically, we generate bubbles with $R_b \approx 30$ µm by setting $p = 48.3$ kPa and $q = 10$ µL/s. The downstream reservoir of the flow-focusing device is connected to a 12 or 24 mL syringe with a 0.3 mm diameter PTFE tube. Bubbles accumulate in the syringe, which is capped at its end. Then, the piston is added at the top of the filled syringe. By weighing the syringe and measuring the foam volume, we deduce the foam liquid fraction $\epsilon = 0.2 \pm 0.05$.

For the injection stage, we use the pre-generated foam cartridge on the experimental set-up presented in the first section. We reproduce the same protocol with a range of foam flow rates Q between 15 µL/min (0.9 mL/h) and 1000 µL/min (60 mL/h). We also use the same oils in the porous substrates, as well as the same channel geometry.

Results and discussion

We report a typical time series of the extraction process by an aqueous foam in Fig. 8a. We observe a non-uniform extraction front for all of our experiments. In Fig. 8c-f, we represent α as a function of Qt by varying Q, R_b and H. In particular, we report a surprising feature: an increase of flow rate engenders a decrease of α for a given injected volume with all other parameters constant. In other words, the slower the injection, the more efficient the oil extraction. Moreover, Fig. 8e shows that the bubble radius has no influence on the extraction profile. If we compare α in the foam-driven case to the surfactant-driven case (Fig. 8f), α is higher in the foam case for a given injected volume. This result is all the more surprising as the injection flow rates Q used for the aqueous foams are one to two orders of magnitude lower than those used for surfactant solutions.

To understand these results, we note that with aqueous foams, the applied shear stress is higher than with surfactant solutions. Indeed, as sketched in Fig. 8b, the existence of a thin film between the foam bubbles and the underlying oil layer creates a higher shear stress, since the velocity gradient does not apply on the channel height H but rather occurs over the film thickness D. Owing to their chemical composition, the bubbles have rigid air-water interfaces[25] that act as a rigid wall for the oil layer. Thus, we model the shear stress exerted by the foam on the oil phase as $\tau_{xy}^{foam} = \eta_w Q/(WHD)$. Replacing τ_{xy} in Eqs. (2a - 2b) with τ_{xy}^{foam}, we obtain a new expression for α(t):

$$\alpha + (1-\alpha_\infty)\log\left(\frac{\alpha_\infty}{\alpha_\infty - \alpha}\right) = \frac{c_s h}{WHDL_o}\frac{\eta_w}{\eta_o}\frac{1}{c_d}Qt \tag{4a}$$

$$\alpha_\infty = 1 - \frac{2c_p}{c_s}\frac{D}{L_o}\frac{h}{w}\frac{\cos\theta}{Ca} \quad . \tag{4b}$$

In order to use Eqs. (4a - 4b), we measure θ and use D as an adjustable parameter. Again, like for surfactant solutions, θ depends on Ca. More precisely, as shown in Fig. 9a, we can collapse all the angle measurements from surfactants and foams on the same plot

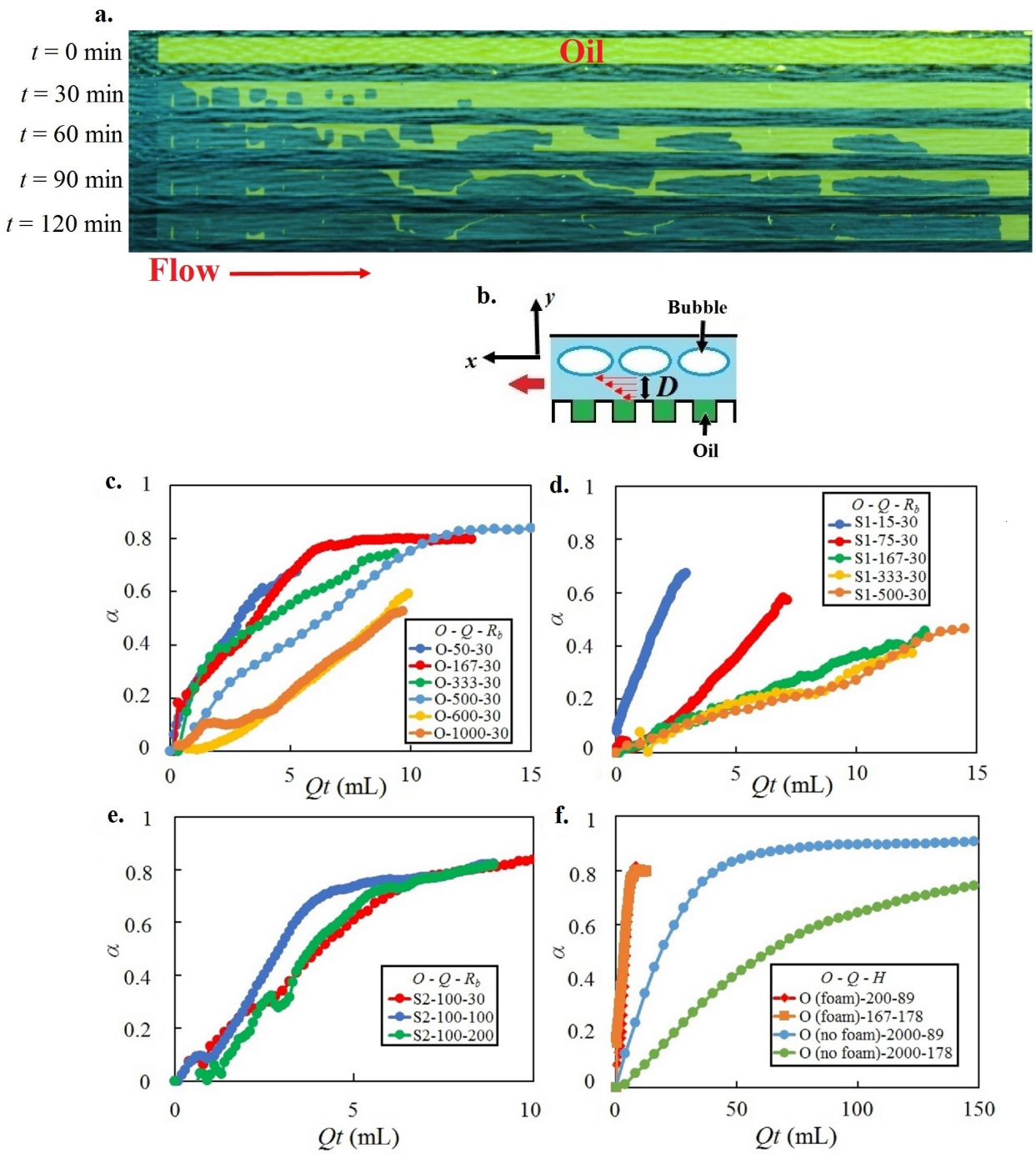

Figure 8: a. Top-view of olive oil extraction by an aqueous foam with $R_b = 100$ μm and $Q = 50$ μL/min. Fluorescent dyed oil appears green-yellow. The flow is from left to right. b. Foam flow in the channel with D, the film thickness between the substrate and the bubbles. c - f. Efficiency α as a function of the injected volume Qt for different systems: c. Olive oil extraction by a foam with $R_b = 30$ µm. d. Silicon oil 1 extraction by a foam with $R_b = 30$ µm. e. Extraction for silicon oil 2 and $R_b = 30$, 100 and 200 µm, and $H = 179$ µm. f. Comparison between surfactant solutions and foams with a varying channel height (89 or 178 µm). In the legend, O, Q (µL/min), R_b (µm) and H (µm) are, respectively, the oil type, the injection flow rate, the mean bubble radius and the channel height.

by introducing a new capillary number $\tilde{Ca} = Ca(H/\ell)$ where ℓ is the characteristic length for viscous dissipation. If $\ell = H$ for surfactant solutions, then $\tilde{Ca} = Ca$, and $\ell = D$ for foams. Fig. 9b-c compares α_{exp} and $f(\alpha_{exp})$ to $G(t) = \frac{c_s h}{WHDL_o}\frac{\eta_w}{\eta_o}\frac{1}{c_d}Qt$. We are able to obtain good agreement between Eqs. (4a - 4b) and our data sets.

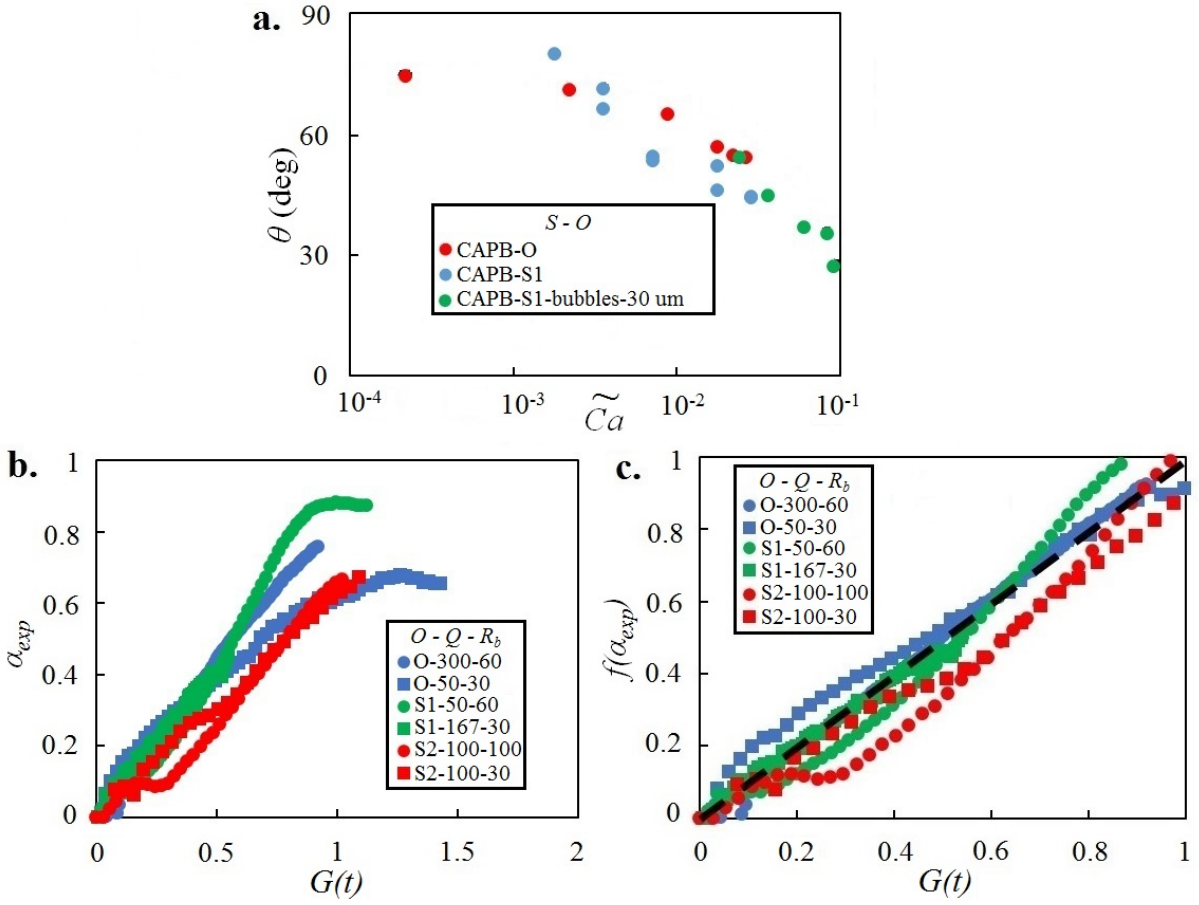

Figure 9: a. Measurements of the receding contact angle θ as a function of $\tilde{Ca}$. b. Experimental efficiency α_{exp} as a function of $G(t) = \frac{c_s h}{WHDL_o}\frac{\eta_w}{\eta_o}\frac{1}{c_d}Qt$ for some oils, Q (µL/min) and R_b (µm). c. $f(\alpha_{exp})$ as a function of $G(t)$ for the same parameters. $f(\alpha_{exp}) = G(t)$ is represented by the black dashed line.

The fitting parameter D is found to vary between 1 µm and 7 µm, as shown in the inset of Fig. 10a. The values of D are in reasonable agreement with common orders of magnitude found for a bubble moving across a solid wall.[42–46] Also, we notice that D and τ_{xy}^{foam} do not depend strongly on R_b, since $\alpha(Qt)$ maintains the same profile when we increase R_b by 10 times (Fig. 8e). More precisely, we compare the results for D to the estimations of film thickness provided by mathematical studies of the liquid meniscus

at a solid wall. To do so, we introduce the dimensionless film thickness $D^* = D/H$ and the dimensionless applied shear stress $\tau_{xy}^{foam*} = \tau_{xy}^{foam} H/\gamma_{aw}$ by non-dimensionalizing D and τ_{xy}^{foam}, respectively, by H and by γ_{aw}/H. In Fig. 10, we plot D^* and τ_{xy}^{foam*} as a function of the outer capillary number $Ca^* = \eta_w Q/(WH\gamma_{aw})$ that differs from Ca by replacing γ_{ow} by the air-water interfacial tension γ_{aw}. We find a good collapse with the exact solution for wet foams, made with the combination of surfactants and fatty acids used in our experiments and developed by Denkov et al.[42–44] in the limit of wet foams. In their study, they find:

$$D^* = Ca^{*1/2} \tag{5a}$$

$$\tau_{xy}^{foam^*} = 4.63\xi(\epsilon)Ca^{*1/2} + 7.35\chi(\epsilon)Ca^{*2/3} \tag{5b}$$

where ξ and χ are functions of the liquid fraction ϵ. Common surfactant-based foams with poor rigidity and shorter lifetime, such as SDS or TTAB, exhibit the classical Bretherton theory[47] for $D \propto Ca^{*2/3}$ on a bubble moving in a channel of comparable size. This scaling can be derived by balancing the pressure gradient in the meniscus at the bubble front with the viscous dissipation at the wall. In the exact calculations, friction is neglected in the central area of the film. However, the calculations by Denkov et al. are based on the assumption of rigid tangentially immobile interfaces, which means that the velocities of the upper film surface and the wall are different and creates friction. Thus, it gives a difference of power laws (Eqs. (5a - 5b)). While they consider the bubble radius R_b and the capillary pressure in the bubbles γ_{aw}/R_b as the rescaling parameters, we use H as the characteristic length. One possible reason is that the confinement of the bubbles in the channel sets a different and unique characteristic length, which is the channel height H.

Since D is smaller when Ca^* decreases, this explains why smaller flow rates are more favourable to drain oil out for a given injected volume (see Eq. (4a)). This result can also be interpreted as a longer contact time between the foam and the lubricating liquid when injection is slow.

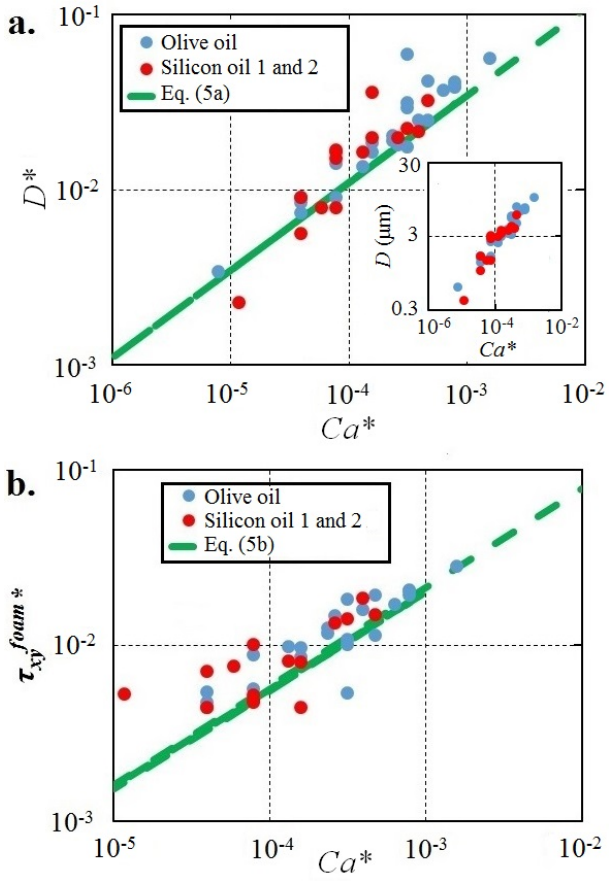

Figure 10: a. Dimensionless film thickness $D^* = D/H$ as a function of the outer capillary number Ca^* for all data sets with $H = 89$ or 178 μm. Inset: Film thickness D as a function of Ca^* for the same data set. b. Dimensionless applied shear stress $\tau_{xy}^{foam*} = \tau_{xy}^{foam} H/\gamma_{aw}$ as a function of Ca^* for all data sets. The green dashed line represents the values predicted by Denkov et al.[43] with H as a rescaling length.

Summary and conclusions

In this paper, we have shown that surfactants in the outer phase have a strong impact on the standard shear-driven oil extraction and drainage from liquid-infused surfaces. First, surfactants adsorb at the oil-water interface. Thus, they change the dynamics of the contact line between the posts that make up the porous substrate. Second, the adsorption of surfactants can trigger long-wave and short-wave instabilities at the oil-water interface, leading to the non-uniform propagation of the extraction front.

Furthermore, using aqueous foams (like in most recovery processes) in the outer phase changes extraction dynamics drastically. The existence of a thin water film between the

foam and the oil phase increases the shear exerted by the outer phase. Thus, it also decreases by up to two orders of magnitude the typical injection flow rates required to extract oil completely out of the channel. The decreasing value of the film thickness when the outer capillary number Ca^* is reduced also means that lower flow rates increase the efficiency of oil recovery for a given injected volume of foam.

In conclusion, we show that the shear-driven drainage of slippery liquid-infused surfaces by surfactant solutions and aqueous foams can be understood with the theoretical arguments developed by Wexler et al. for pure aqueous phases.[1] However, the chemical and physical nature of the external flow modifies the dynamics of the receding contact line and/or the nature of the applied shear stress. In both cases, we account for these interfacial effects by introducing a modified dependence on the capillary numbers Ca and Ca^*. The failure of the liquid-infused surfaces is enhanced when the interfacial capillary number Ca is increased for surfactant solutions, especially by the reduction of the oil-water interfacial tension. In the foam case, decreasing Ca^* for a given injected volume of foam enhances the oil extraction and the subsequent failure.

Acknowledgement

The authors thank I. Cantat, F. Gallaire, H. Kim and S. Shin for their helpful discussions, the interfacial tension measurements and the microfabrication. We also thank the Department of Mechanical and Aerospace Engineering at Princeton University and Paris-Est University - Navier Institute for their financial support.

References

(1) Wexler, J. S.; Jacobi, I.; Stone, H. A. Shear-driven failure of liquid-infused surfaces. *Phys. Rev. Lett.* **2015**, *114*, 168301.

(2) Lafuma, A.; Quéré D. Slippery pre-suffused surfaces. *Europhys. Lett.* **2011**, *96*, 56001.

(3) Smith J. D.; Dhiman R.; Anand S.; Reza-Garduno E.; Cohen R. E.; McKinley G. H.; Varanasi K. K. Droplet mobility on lubricant-impregnated surfaces. *Soft Matter* **2013**, *9*, 1772-1780.

(4) Epstein A. K.; Wong T. S.; Belisle R. A.; Boggs E. M.; Aizenberg J. Liquid-infused structured surfaces with exceptional anti-biofouling performance. *Proc. Natl. Acad. Sci.* **2012**, *109*, 13182.

(5) Wong T. S.; Kang S. H.; Tang S. K. Y.; Smythe E. J.; Hatton B. D.; Grinthal A.; Aizenberg J. Bioinspired self-repairing slippery surfaces with pressure-stable omniphobicity. *Nature* **2011**, *477*, 443.

(6) Anand S.; Paxson A. T.; Dhiman R.; Smith J. D.; Varanasi K. K. Enhanced condensation on lubricant-impregnated nanotextured surfaces. *ACS Nano* **2012**, *6*, 10122-10129.

(7) Xiao R.; Miljkovic N.; Enright R.; Wang E. N. Immersion condensation on oil-infused heterogeneous surfaces for enhanced heat transfer. *Scientific Reports* **2013**, *3*, 1988.

(8) Kim P.; Wong T.S.; Alvarenga J.; Kreder M. J.; Adorno-Martinez W.; Aizenberg J. Liquid-infused nanostructured surfaces with extreme anti-ice and anti-frost performance. *ACS Nano* **2012**, *6*, 6569.

(9) Busse A.; Sandham ND.; McHale G.; Newton M. I. Change in drag, apparent slip and optimum air layer thickness for laminar flow over an idealised superhydrophobic surface. *J. Fluid. Mech.* **2013**, *727*, 488-508.

(10) Jacobi, I.; Wexler J. S.; Stone H. A. Overflow cascades in liquid-infused substrates. *Phys. of Fluids* **2015**, *27*, 082101.

(11) Lenormand, R.; Zarcone, C.; Sarr, A. Mechanisms of the displacement of one fluid by another in a network of capillary ducts. *J. Fluid Mech.* **1983**, *135*, 337-353.

(12) Bonnet, J.; Lenormand, R. Constructing micromodels for the study of multiphase flow in porous media. *Oil and Gas Sci. Tech.* **1977**, *32*, 477-480.

(13) Dake L. P. Fundamentals of Reservoir Engineering. *Elsevier*, **1978**.

(14) Kornev, K. G.; Neimark, A. V.; Rozhkov, A. N. Foam in porous media: thermodynamic and hydro dynamic peculiarities. *Adv. Col. Int. Sci.* **1999**, *82*, 127-187.

(15) Farajzadeh R.; Andrianov A.; Krastev R.; Hirasaki G. J.; Rossen W. R. Foam-oil interaction in porous media: implications for foam assisted enhanced oil recovery. *Adv. Col. Int. Sci.* **2012**, *183*, 1-13.

(16) Mulligan C.; Wang S. Remediation of a heavy metal-contaminated soil by a rhamnolipid foam. *Eng. Geology* **2006**, *85*, 75-81.

(17) Wang S.; Mulligan C. An evaluation of surfactant foam technology in remediation of contaminated soil. *Chemosphere* **2004**, *57*, 1079-1089.

(18) Conn C.; Ma K.; Hirasaki G. J.; Biswal S. Visualizing oil displacement with foam in a microfluidic device with permeability contrast. *Lab on a Chip* **2014**, *14*, 3968.

(19) Jones S. A.; Dollet B.; Slosse N.; Jiang Y.; Cox S. J.; Graner F. Two-dimensional constriction flows of foams. *Col. and Surf. A: Phys. and Eng. Asp.* **2011**, *382*, 18-23.

(20) Quennouz N.; Ryba M.; Argillier J-F.; Herzhaft B., Peysson Y. and Pannacci N. Microfluidic study of foams flow for enhanced oil recovery (EOR). *Oil and Gas Sci. Tech.* **2014**, *69*, 457-466.

(21) Bartolo D.; Degré G.; Nghe P.; Studer V. Microfluidic stickers. *Lab on a Chip* **2008**, *8*, 274.

(22) Shah R. K.; London A. L. Laminar Flow Forced Convection in Ducts. *Academic Press*, New York, 1978.

(23) Bartolo D.; Bouamrirene D.; Verneuil E.; Buguin A.; Silberzan P.; Moulinet S. Bouncing or sticky droplets: Impalement transitions on superhydrophobic micropatterned surfaces. *Europhys. Lett.* **2006**, *74*, 299-305.

(24) Basheva E.; Ganshev D.; Denkov N. D.; Kasuga K.; Satoh N.; Tsujii K. Role of betaine as foam booster in the presence of silicone oil drops. *Langmuir* **2006**, *16*, 1000.

(25) Golemanov K.; Denkov N. D.; Tcholakova S.; Vethamuthu M.; Lips A. Surfactant mixtures for control of bubble surface mobility in foam studies. *Langmuir* **2008**, *24*, 9956-9961.

(26) Fermigier M.; Jenffer P. An experimental investigation of the dynamic contact angle in liquid-liquid systems. *J. Col. Int. Sci.* **1991**, *146*, 226-241.

(27) Tanner L. H. The spreading of silicone oils on horizontal surfaces. *J. Phys. D* **1979**, *12*, 1473.

(28) Hoffmann R. L. A study of the advancing interface. I. Interface shape in liquid - gas systems. *J. Col. Int. Sci.* **1975**, *50*, 228.

(29) de Gennes P. G. Wetting: statics and dynamics. *Rev. Mod. Phys. Sci.* **1985**, *57*, 827.

(30) de Gennes P. G.; Brochard - Wyart F.; Quéré D. Capillarity and Wetting Phenomena: Drops, Bubbles, Pearls and Waves. *Springer*, **2004**.

(31) Cox R. G. The dynamics of the spreading of liquids on a solid surface. Part 1. Viscous flow. *J. Fluid Mech.* **1986**, *168*, 169-194.

(32) Huh C.; Scriven L. E. Hydrodynamic model of steady movement of a solid/liquid/fluid contact line. *J. Col. Int. Sci.* **1971**, *35*, 85-101.

(33) Yih C. S. Instability due to viscous stratification. *J. Fluid Mech.* **1967**, *27*, 337-352.

(34) Hooper A. P.; Boyd W. G. C. Shear-flow instability at the interface between two viscous fluids. *J. Fluid Mech.* **1983**, *128*, 507-528.

(35) Charru F.; Hinch E. J. "Phase diagram" of interfacial instabilities in a two-layer Couette flow and mechanism of the long-wave instability. *J. Fluid Mech.* **2000**, *414*, 195-223.

(36) Frenkel A. L.; Halpern D. Stokes-flow instability due to interfacial surfactant. *Phys. Fluids* **2000**, *14*, 45-48.

(37) Blyth M. G.; Pozrikidis C. Effect of surfactants on the stability of two-layer channel flow. *J. Fluid Mech* **2004**, *505*, 59-86.

(38) Troian S. M.; Herbolzheimer E.; Safran S. A.; Joanny J. F. Fingering instabilities of driven spreading films. *Europhys. Lett.* **1989**, *10*, 25-30.

(39) Garstecki P.; Stone H. A.; Whitesides G. Mechanism for flow-rate controlled breakup in confined geometries: a route to monodisperse emulsions. *Phys. Rev. Lett.* **2004**, *94*, 164501.

(40) Garstecki P.; Gitlin I.; DiLuzio W.; Whitesides G.; Kumacheva E.; Stone H. A. Formation of monodisperse bubbles in a microfluidic flow-focusing device. *App. Phys. Lett.* **2004**, *85*, 13.

(41) Saint-Jalmes A. Physical chemistry in foam drainage and coarsening. *Soft Matter* **2006**, *2*, 836-849.

(42) Denkov N. D.; Tcholakova S.; Golemanov K.; Ananthpadmanabhan K. P.; Lips A. The role of surfactant type and bubble surface mobility in foam rheology. *Soft Matter* **2009**, *5*, 3389-3408.

(43) Denkov N. D.; Subramanian V.; Gurovich D.; Lips A. Wall slip and viscous dissipation in sheared foams: effect of surface mobility. *Col. and Surf. A* **2005**, *263*, 129-145.

(44) Denkov N. D.; Tcholakova S.; Golemanov K.; Subramanian V.; Lips A. Foam-wall friction: effect of air volume fraction for tangentially immobile bubble surface. *Col. and Surf. A* **2006**, *282*, 329-347.

(45) Cantat I. Liquid meniscus friction on a wet plate: Bubbles, lamellae, and foams. *Phys. Fluids* **2013**, *25*, 031303.

(46) Le Merrer M.; Lespiat R.; Hohler R.; Cohen-Addad S. Linear and non-linear wall friction of wet foams. *Soft Matter* **2015**, *11*, 368-381.

(47) Bretherton F. P. The motion of long bubbles in tubes. *J. Fluid. Mech.* **1961**, *10*, 166.

(48) Lenormand R.; Touboul E.; Zarcone C. Numerical models and experiments on immiscible displacements in porous media. *J. Fluid Mech.* **1988**, *189*, 165-187.

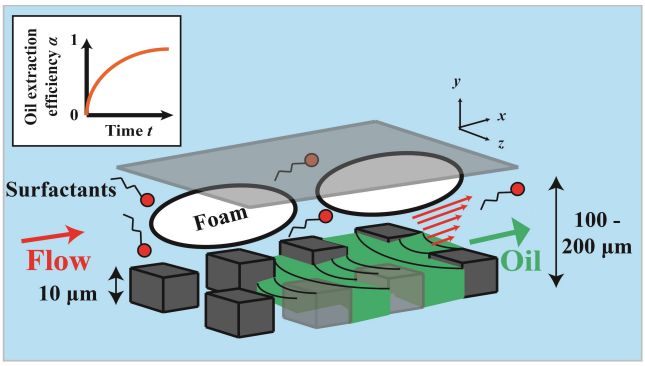

Figure 11: For Table of contents only